Insights into the reaction mechanism for 5-hydroxymethylfurfural oxidation to FDCA on bimetallic Pd-Au nanoparticles

# Insights into the reaction mechanism for 5-hydroxymethylfurfural oxidation to FDCA on bimetallic Pd-Au nanoparticles

Alice Lolli[a,b], Stefania Albonetti[a,b,*], Luca Utili[a], Rossella Amadori[a], Francesca Ospitali[a], Carlo Lucarelli[b,c], Fabrizio Cavani[a,b,*]

a Dip. Chimica Industriale "Toso Montanari", Università di Bologna, Viale Risorgimento 4, 40136 Bologna (BO), Italy

b Consorzio INSTM - UdR Bologna, Via G. Giusti, 9 - 50121 Florence, Italy

c Dipartimento di Scienza e Alta Tecnologia, Università degli studi dell'Insubria, Via Valleggio 11, 22100 Como

* Corresponding authors: Phone +390512093680 – E-mail address fabrizio.cavani@unibo.it
Phone +390512093681 – E-mail address stefania.albonetti@unibo.it

## Abstract

This work deals with the oxidation of 5-hydroxymethylfurfural (HMF) to 2,5-furandicarboxylic acid (FDCA) in water using supported Pd-Au nanoparticles. The active phase composition was shown to be crucial for FDCA formation. Indeed, both Au and Pd monometallic nanoparticles formed 5-hydroxymethyl-2-furancarboxylic acid (HMFCA) under the studied conditions; however, with Pd nanoparticles HMFCA was not further transformed, while Au and bimetallic Pd-Au systems both catalysed its oxidation to FDCA.

The thermal treatment of Pd-Au catalysts considerably modified their catalytic activity, because Pd atoms migrated and concentrated onto the outer part of bimetallic nanoparticles. The resulting active phase morphology showed a different reaction path for FDCA formation compared to the untreated catalyst, with an important contribution of the Cannizzaro reaction. PVP-protected Pd-Au nanoparticles with different structures (either alloy or core-shell morphology) were synthesized and their reactivity tested in order to confirm the presence of different mechanisms for HMF oxidation, depending on whether the active phase preferentially exposes either Pd or Au atoms.

## 1. Introduction

Biomasses are currently the most promising alternative to fossil sources for the production of fuels and chemicals [1,2]. In the transformation of biomass into chemicals, an important role is played by furfural derivatives that have functional groups in position five [3,4]. For instance, 5-hydroxymethyl-2-furfural (HMF) is a key precursor for the synthesis of derivatives with application

in the pharmaceutical and polymer industries [5-8]. This molecule can be oxidized to obtain 2,5-furandicarboxylic acid (FDCA), a monomer for the synthesis of a new class of polymers, alternative to those obtained from terephthalic acid. As an example, Avantium is using FDCA to produce polyethylene furandicarboxylate (PEF); the exact route for the synthesis of FDCA has not yet been disclosed, but the current technology for terephthalic acid production using metal/bromide catalysts is probably being evaluated. One drawback of these catalytic systems is the use of corrosive media and dangerous compounds, which make the process polluting [9-11]. Moreover, there are concerns regarding the purity of both the product and the final polymer.

Recently Au-supported catalysts were found to be very active for HMF oxidation to FDCA [12,13]. Many researchers have focused their attention on the study of the best material and reaction conditions for improving FDCA yield [14-17]. So far, catalyst stability and productivity are low, but the possibility to obtain both high product purity and better process sustainability makes this catalyst type highly interesting.

According to the current state of the research, the use of bimetallic catalysts with controlled size and composition may be a promising way to improve catalyst activity and stability [18,19]. In our previous studies [18,20], we synthesized titania-supported Au and Au-Cu nanoparticles by using PVP-stabilized sols with controlled size, structure and composition. Unprecedented catalytic activity and stability were obtained with these catalytic materials in the oxidation of HMF to FDCA.

The combination of Pd and Au was also shown to be very successful in producing active and selective catalysts [19,21]. This bimetallic system has been widely studied for a number of different applications [22,23]. In particular, Prati and co-workers [24-26] and Hutchings and co-workers [27,28] have demonstrated that the supported Pd-Au alloy shows excellent performances for many oxidation reactions such as the selective oxidation of alcohols and the synthesis of $H_2O_2$ from $H_2$ and $O_2$.

Pd-Au nanoparticles can develop morphologies ranging from core-shell to homogeneous alloys, depending on the method of synthesis and thermal treatment of the catalysts [29]. The Pd-Au alloy most frequently used in catalytic applications contains a bulk Au:Pd molar ratio of 1:1. However, it has been documented that the concentration of the metals at the nanoparticles surface may differ from that of the bulk. Notably, Pd may migrate and concentrate in the outer part of the particles, so developing a core-shell structure [30,31]; this phenomenon may significantly influence the catalytic activity.

In the present study, the role of the active phase and the effect of catalyst calcination were studied for the liquid-phase oxidation of HMF using Pd-Au catalysts. We synthesized nanoparticles with different Au:Pd atomic ratios and morphologies, in order to investigate the effect of these parameters on the catalytic activity and product selectivity.

The results obtained indicate that different reaction paths may take place in the presence of either a homogeneous Pd-Au alloy or of an active phase exposing preferentially monometallic species. Therefore, core-shell nanoparticles were also synthesized in order to investigate on differences in the reaction mechanism due to the formation of a distinct morphology.

## 2. Experimental

### 2.1 Materials

The following reagents and products were used for catalyst synthesis and for reactions: polyvinylpyrrolidone (PVP K25, m.w. 29,000 Sigma Aldrich), Sodium hydroxyde (Sigma Aldrich), $HAuCl_4*3H_2O$ (Sigma Aldrich), $PdCl_2$ (Sigma Aldrich), β-D-Glucose (Fluka), $TiO_2$ anatase (DT51 Millennium Chemicals), 5-hydroxymethyl-2-furfural (Alfa Aesar), 2,5-furandicarboxylic acid (Toronto Research Chemicals), 5-hydroxymethyl-2-furan carboxylic acid (Toronto Research Chemicals), 5-formyl-2-furan carboxylic acid (Toronto Research Chemicals), 2,5-diformylfuran (Toronto Research Chemicals), and 2,5-Bis(hydoxymethyl)furan (Toronto Research Chemicals).

### 2.2 Catalyst preparation

$Au/TiO_2$, $Pd/TiO_2$, and $Au\text{-}Pd/TiO_2$ catalysts were prepared by the immobilization on the $TiO_2$ surface of the preformed monometallic and bimetallic colloids. Mono- and bimetallic nanoparticles were prepared using a method previously described [18,20,32-34]. In brief, the necessary quantity of polyvinylpyrrolidone, used as a nanoparticle stabilizer, was added to a solution of NaOH in water. The solution was then heated to 95°C. At this temperature, β-D-glucose and an aqueous solution containing the metal precursors ($HAuCl_4$ and $PdCl_2$) in the desired ratio were added and stirred for 2.5 min. Some drops of HCl were added to this solution in order to increase the solubility of the Pd salt. The ratio among PVP, β-D-glucose, NaOH, and metals was optimized for each gold and palladium content, taking into consideration the procedure used for other bimetallic systems [35-37]. Core-shell nanoparticles were prepared from a monometallic system (Au or Pd), synthesized following the previous strategy, which had been used as seed for the nucleation of the second metal. In order to form the shell structure, the second metal was added once the nanoparticles of the first metal were formed. The quantity of organic reagents and base was the same as that used for bimetallic systems.

Before use, the as-prepared sols were concentrated and washed with distilled water using 50 and 30 kDa Amicon Ultra filters (Millipore) to eliminate the excess PVP and other reagents dissolved in the aqueous media. Then Pd and Pd-Au colloids were impregnated onto $TiO_2$ by maintaining the total metal loading at 1.5 wt%, while the ratio Pd:Au was varied from 3:1 to 1:9 on a molar basis. For

all samples the impregnation solvent was evaporated by thermal treatment at 120°C. Samples were also calcined at 300°C to study the effect of calcination on their activity. Catalyst samples are denoted as Au-$TiO_2$, Pd-$TiO_2$, and $Pd_xAu_y$-$TiO_2$, where x and y refer to the Pd:Au molar ratio in the material (i.e. $Pd_1Au_1$-$TiO_2$ indicates a $TiO_2$-supported sample synthesized with 1.5 wt% total metal and with a Pd:Au molar ratio of 1). The corresponding preformed nanoparticles were also studied. Table 1 compiles the composition and characteristics of the catalysts investigated in this work.

### 2.3 Oxidation reactions

The oxidation of 5-hydroxymethyl-2-furfural (HMF) was carried out using an autoclave (Parr Instruments) reactor with 100 mL capacity, equipped with a mechanical stirrer (0–600 rpm) and temperature and pressure gauges [38]. The reactor was charged with an aqueous solution (25 mL distilled water) containing the appropriate amount of HMF, base (NaOH), and catalyst (HMF/metal molar ratio = 100). The autoclave was purged 3 times with $O_2$ (5 bar) and then pressurized at 10 bar. Unless indicated otherwise, the temperature was increased to 70ºC and the reaction mixture was stirred at approximately 400 rpm for 4 h. The initial time (time 0) for the reaction was taken when the set point temperature was reached (after 8 min of heating). At the end of the reaction, the reactor was cooled down to room temperature and the solution was filtered. When colloids were used as catalysts, the reaction mixture was separated using 30 kDa and 50kDa Amicon Ultra filters (Millipore). Then 4 mL of water were added to an aliquot of the reaction solution (1 mL) before analysis with an Agilent Infinity 1260 liquid chromatograph equipped with an Aminex HPX 87-H 300 mm x 7.8 mm column using a 0.005 M $H_2SO_4$ solution as the mobile phase. The compound identification was achieved by calibration using reference commercial samples.

### 2.4 Analytical methods

XRD and HR-TEM analyses were carried on both colloids and impregnated catalysts to verify particle sizes. XRD measurements were carried out at room temperature with a Bragg/Brentano diffractometer (X'pertPro PANalytical) equipped with a fast X'Celerator detector, using a Cu anode as the X-ray source (Kα, λ=1.5418 Å). For all sols, diffractograms were recorded in the range 35-44°2θ, counting for 1000 s every 0.1° 2θ step. This made it possible to evaluate the coherence length of the Pd crystalline domain through a single-line profile fitting of the reflection at 2θ 40.4°, as well as to check the Au characteristic reflection at 2θ 38.2°. Crystallite size values were calculated using the Scherrer equation. The lattice parameter values were calculated from the (111) peak of the face-centred cubic (fcc) nanoparticles. For catalysts, complete diffractograms were recorded over the 10-80° 2θ range, counting for 20 s every 0.05° 2θ step. However, for the evaluation of the metal

crystallite size, a second acquisition was performed in the 40-46° 2θ range, counting for 1500 s at each 0.08° 2θ step. For catalysts with a high Au content, crystallite size values were calculated using the Au reflection peak at 2θ 44.3°. It was not possible to calculate crystallite sizes on the main Pd reflection peaks (2θ 40.3 and 46.9°) because of the presence of anatase peaks in the same position.

Nanoparticle suspensions and catalysts were also examined by high resolution transmission electron microscopy (HR-TEM) using a TEM/STEM FEI TECNAI F20, which uses a high-angle annular dark field (HAADF) imaging mode at 200kV and with an EDS PV9761N SUTW energy dispersive X-ray spectrometer (EDX) for X-ray microanalysis. The samples were dispersed on a holey carbon film supported on a copper grid.

Catalyst surface areas were measured by one $N_2$ physisorption apparatus (Sorpty 1750 CE instruments) and single-point BET analysis methods; samples were pre-treated under vacuum at 120°C.

## 3. Results and discussion

### 3.1 Characterization of preformed nanoparticles and catalysts

The preparation of monometallic Pd and Au and bimetallic Pd-Au systems with different molar ratios led to the formation of small and stable particles. The resulting dispersions had a brownish colour, with intensity depending on the composition and Pd content.

Prepared sols were characterized by TEM. Some representative images are presented in Figure 1. Nanoparticles showed a spherical morphology with a mean particle size ranging from 2.5 nm to 5 nm, depending on the sample composition (Table 2). Indeed, TEM measurements demonstrate that the Au sol has larger particles and a broader particle size distribution as compared to the Pd-Au and monometallic Pd sols, suggesting that the addition of Pd to Au decreases particle dimensions.

The X-ray diffraction analysis (Fig. 2) of the bimetallic nanoparticles showed a significant shift of the main reflection when the Pd content was increased in the samples. The binary phase diagram of the Pd-Au system indicates that Au and Pd should exhibit a complete reciprocal solubility. Thus, the observed shift in the 2θ value is consistent with the incorporation of Pd into the Au lattice, indicating that bimetallic nanoparticles have a high degree of alloying.

PVP-protected Pd-Au nanoparticles with core-shell morphology were also synthesized, in order to investigate on the mechanism of FDCA formation when an active phase that preferentially expose either Pd or Au atoms is used. The microstructure of the prepared $Pd_1@Au_6$ (Pd core) and $Au_6@Pd_1$ (Au core) core-shell catalysts was investigated using TEM, STEM, and EDX to confirm the distribution of metals within bimetallic particles. Figures 3, 4 and 5 show TEM images and particle size distribution of core-shell and alloyed samples, and the compositional mappings of Pd and Au.

Core-shell nanoparticles (Figures 3a and 4a) have a sphere-like shape and their average diameter is 3.7 nm for $Pd_1@Au_6$ and 7.4 nm for $Au_6@Pd_1$, similar to the shape and dimension of the core metal. Alloy nanoparticles ($Pd_1Au_6$) have an average diameter of 3.9 nm. Figures 3b, 4b and 5b depict the HAADF-STEM elemental mapping of Pd, Au, and their overlapping for $Pd_1@Au_6$, $Au_6@Pd_1$ and $Pd_1Au_6$ nanoparticles; these results confirm that the particles show a morphology with either an Au-rich shell, or an Au-rich core or an Au-Pd alloy, respectively. Indeed, the signals of both Pd and Au can be clearly observed in elemental mapping images, indicating that both of the atoms are distributed within the whole nanoparticles with a concentration gradient which differed depending on the preparation method used. In the case of the $Pd_1@Au_6$ sample (Fig. 3b), the analysis suggests that Pd was the predominant element in the inner part of nanoparticles, while Au was present on the particles surface. Conversely, with $Au_6@Pd_1$ (Fig. 4b), the opposite trend was shown, further proving the predominance of Pd atoms on the surface of this catalyst. The low amount of Pd in the system prevented the formation of a well-defined shell; nevertheless, the Pd:Au ratio was clearly higher on the nanoparticle surface as compared to the core. Finally, in the case of $Au_6Pd_1$ nanosol (Fig. 5b) the complete overlapping of Pd and Au signals was shown, which confirms the presence of an homogeneous alloy.

All the synthesized nanoparticles, except for the core-shell systems, were deposited on $TiO_2$ by incipient wetness impregnation, with a metal loading of 1.5 wt.%. BET analysis (Table 1) showed a decrease of the surface area value when the Pd content was increased. This effect was probably due to the higher organic content, necessary for the synthesis of small and stable Pd particles. Indeed, a greater amount of PVP may occlude the porosity of the support, when the suspension is deposited over the surface, as also shown for the Au-Cu system [18,20]. All supported catalysts, both after drying and calcination, were characterized by XRD analysis. As an example, Fig. S1 shows the XRD pattern of both dried and calcined $Pd_1Au_6$-$TiO_2$ sample; however, the information obtained from this analysis on the structure of the metallic phase are poor and no clear indication can be obtained from these data.

The TEM analysis of selected supported nanoparticles and their size distribution histograms are shown in Figure 6. The measurement of randomly chosen nanoparticles over the support confirmed that particles with a greater Au content had larger dimensions than Pd particles. Nevertheless, the metal phase was still characterized by dimensions between 3.4 nm and 6.9 nm, thus suggesting that the impregnation of metal sols on the $TiO_2$ support (Fig. 6a, 6b) and calcination (Fig. 6c) generates a high metal dispersion and does not significantly affect the active phase dimension.

**3.2 Catalytic Tests**

The synthesis of FDCA by means of HMF oxidation has been widely studied over the past two decades using different reaction conditions and catalysts [11,17]. Scheme 1 shows the general HMF oxidation pattern. FDCA is usually produced in two stages: the carbonylic group is first oxidized to the carboxylic moiety, producing 5-hydroxymethyl-2-furancarboxylic acid (HMFCA); then, typically, the oxidation of the hydroxymethyl group in HMFCA yields FDCA through 5-formyl-2-furancaboxylic acid (FFCA) as the intermediate [39]. Furthermore, sometimes the formation of 2,5-diformylfuran (DFF) was also observed, mainly in the absence of an added base and with metals other than Au [40].

*3.2.1 Effect of catalysts composition*

Both monometallic and bimetallic systems were tested as catalysts for HMF oxidation. First, the reaction was carried out on monometallic Au and Pd systems, in basic water, at different temperatures and with different NaOH contents (Table 3). The results indicate that the Pd-$TiO_2$ catalyst is less active than Au-$TiO_2$ in FDCA formation. Indeed, with both catalysts and under similar reaction conditions, most of the reagent was transformed into HMFCA, but Pd-$TiO_2$ produced a slightly lower amount of FDCA than Au-$TiO_2$ (selectivity 8% vs. 12%). Moreover, FDCA yield remained almost unchanged when the amount of NaOH in the reaction was increased with Pd-$TiO_2$, whereas the Au-$TiO_2$ activity was significantly influenced by the base amount. This trend confirms previous results reporting that Pd catalysts are less affected by NaOH concentration than Au catalysts [41]. However, the presence of the base is fundamental also when Pd is used, since in neutral conditions there was no reaction at all. This finding is consistent with previous works [13,42] on metal-supported catalysts, in which the presence of a base is reported to facilitate the deprotonation of alcohol and to promote its conversion into the aldehyde.

In order to gain information on the reaction network, the effect of reaction time in HMF oxidation was investigated. Figure 7 shows HMF conversion and products selectivity plotted in function of time, for the Pd-$TiO_2$ catalyst. HMFCA formation was very fast under the conditions used; indeed, the complete transformation of HMF to HMFCA was obtained after just 30 min reaction time. However, the catalyst was very poorly active for the subsequent oxidation of HMFCA into FDCA, in fact yields to both HMFCA and FDCA were almost unchanged between 30 and 240 min time, which indicates that Pd is unable to promote the oxidation of HMFCA. Similar results were reported by Villa et al. [19] using Pd/C catalysts; these authors ascribed the observed trend to sample deactivation. Conversely, in our study the deactivation of the Pd-$TiO_2$ catalyst may be ruled out, since the further addition of HMF after 1 h led to complete HMF conversion and identical selectivity to both HMFCA and FDCA, as shown in the previous experiment.

As a general observation it must be underlined that, under the basic environment used, the less active catalysts also led to the formation of by-products due to HMF degradation [38]. However, for the Pd catalyst the immediate transformation of HMF avoided its degradation, while very pure HMFCA was obtained. This result confirms the need to quickly transform HMF so removing it from the basic reaction medium in order to produce pure FDCA, since the coloured degradation products originated from HMF and not from HMFCA [43,44]. The increase of the reaction temperature, from 70 to 90°C, did not succeed in enhancing Pd-$TiO_2$ catalytic activity (Table 3, entries 5 and 7), in contrast with what previously observed with Au and Au-Cu catalysts (Table 3, entries 8 and 10) [20].

The catalytic behavior of bimetallic Pd-Au catalysts was significantly different from that of monometallic systems; in fact, the distribution of products was strongly affected by the Pd:Au atomic ratio (Figure 8). In particular, the results clearly show the presence of a synergic effect due to the presence of the two metals. An increase in FDCA selectivity was observed by increasing the Au content, until a maximum value was shown at a Pd:Au atomic ratio equal to 1:6 (Pd 8 wt.%, Au 92 wt.%). A further increase of the Au content resulted in a decrease of FDCA selectivity, although all catalysts with high Au content ($Pd_1Au_3$-$TiO_2$, $Pd_1Au_6$-$TiO_2$ and $Pd_1Au_9$-$TiO_2$) were more efficient in the formation of this product. These results confirm the recent data reported by Prati and co-workers – who used Pd-Au nanoparticles supported on activated carbon [19] – for glycerol and alcohol oxidation. Therefore, a small quantity of Pd seems to be adequate to significantly change the electronic properties of Au and enhance the catalytic activity in alcohol oxidation. The characterization of these catalysts revealed both similar nanoparticle dimensions (in the range 4-6 nm) and homogeneous dispersion over the $TiO_2$ support; therefore an effect of metal particles size on the reactivity seems to be unlikely. Conversely, samples with low Pd content presented an alloy structure, and this morphology seems to be the desired one for producing effective catalysts.

As a preliminary conclusion of these reactivity experiments, we can state that the distribution of products in the oxidation of HMF was strongly affected by catalyst composition; Pd-$TiO_2$ was poorly selective to FDCA because of its inability to oxidise HMFCA. Conversely, FDCA yield was strongly increased by incorporating small amounts of Pd in Au nanoparticles.

### *3.2.2 Mechanistic investigations*

In order to gain further insight on the reaction mechanism, the reactivity of the most active catalyst, $Pd_1Au_6$-$TiO_2$, was thoroughly investigated.

Figure 9 shows the HMF conversion and product selectivity in function of reaction time, with the catalyst dried at 120°C. On this sample the conversion of HMF was always complete. During the first 10 min, the major product was HMFCA (50% selectivity), with lower selectivity to both FDCA

and FFCA. The latter product was detected during the initial stage of the reaction, whereas the selectivity to FDCA increased with time. Results indicate that the reaction network consists of the direct and rapid transformation of HMF into HMFCA, while the rate-determining step for FDCA production is the oxidation of the hydroxymethyl group in HMF. Other by-products, such as DFF, were not detected, and after 4 h of reaction time, a FDCA selectivity of 85% was shown. The observed path reflects the reaction scheme usually reported in literature using basic conditions, as it was also observed for Au-$TiO_2$ [18].

Since the catalysts used were synthesized by using PVP-stabilized sols, $Pd_1Au_6$-$TiO_2$ was thermally treated to examine the effect of PVP removal. Previous results [18,20] demonstrated that the PVP over Au and Au-Cu/$TiO_2$ catalysts did not prevent their activity in HMF oxidation. Nevertheless, it has been reported that the ligands chemisorbed on the nanoparticles may decrease catalyst activity [45,46]; therefore, further experiments were conducted in order to clarify this point.

To obtain clean metallic species, the $Pd_1Au_6$-$TiO_2$ sample was calcined at 300°C [38]. TEM results (Figure 6) demonstrate that the Pd-Au-supported nanoparticles almost retained their size (the mean particle size was 7 nm, versus 6 nm obtained with the dried sample). Nevertheless, the thermal treatment significantly changed the catalyst activity (Figure 10), and FDCA selectivity registered after 4 h reaction time was 50% only. With regard to HMF conversion, the calcination treatment also decreased the rate of HMF transformation; in fact, HMF conversion registered after 30 min with the calcined $Pd_1Au_6$-$TiO_2$ sample was 82%. By further increasing the reaction time up to 1 h, the HMF conversion reached 100%, although many differences were observed in the products selectivity as compared to the dried catalyst. In fact, HMFCA, FFCA and FDCA were formed; however, while the transformation of FFCA to FDCA progressed with time, the concentration of HMFCA was constant during the experiment time, a clear indication that this intermediate did not undergo any consecutive transformation. The absence of reactivity for HMFCA with the concomitant increase in FDCA selectivity suggests that the pathway involving the former compound as the reaction intermediate for FDCA formation no longer took place, as already observed for monometallic Pd-$TiO_2$.

Taking into account the fact that the mean particle sizes for dried and calcined samples were very similar (i.e., 6 and 7 nm, respectively), this result suggests that the thermal treatment induces other modifications on the Pd-Au alloy. The significant change of activity, and a behavior similar to that shown by the Pd catalyst, might be ascribed to the de-alloying of Au and Pd, with Pd segregation towards the surface upon calcination. This behaviour was already reported previously, where calcination led either to the production of an alloy with a Pd-rich shell and an Au-rich core, or to the formation of a Pd layer over a bimetallic nanophase [27,47]. Pd can migrate toward the outer part of the bimetallic nanoparticle and eventually form PdO, depending on both the support type and the

nature of the thermal treatment adopted [48]. Nevertheless, tests performed using Pd-$TiO_2$ sample thermally treated at 300°C under different conditions (either under $H_2$ flow, or in air or first in air and then in $H_2$) demonstrated that neither the reduction, nor the calcination plus reduction treatment of the Pd catalyst could enhance FDCA selectivity (Fig. S2). The segregation of Pd and/or PdO on the outer part of bimetallic nanoparticles might explain the change of reaction pathway for FDCA formation, similar to that one observed with monometallic Pd. Indeed, even with the calcined sample the formed HMFCA did not undergo any consecutive transformation. Conversely, FDCA selectivity increased with reaction time and this clearly indicates the presence of a different pathway for its formation. As a matter of fact, the selectivity to FFCA decreased along with the reaction time increase; this might suggest a tandem reaction to FDCA through the formation of DFF and FFCA as intermediates.

For a better understanding of the reaction mechanism, some catalytic tests were conducted on calcined $Pd_1Au_6$-$TiO_2$ using the reaction intermediates as starting reagents (Table 4).

First, a preliminary experiment was carried out by reacting HMF under $N_2$ (Table 4 – entry 1). This experiment made it possible to ascertain the absence of the base-induced disproportionation of HMF (Cannizzaro reaction) to HMFCA and 2,5-bishydroxymethylfuran (BHMF) under the reaction conditions used; however, a significant amount of HMF was degraded and a 57% conversion of HMF was observed after 30 min, producing a brownish solution.

The Cannizzaro transformation is the base-induced disproportionation of an aldehyde lacking a hydrogen atom at α-position to the carbonyl group. One molecule of the aldehyde acts as a hydride donor while the other functions as an acceptor, resulting in the production of an alcohol and a carboxylic acid. This reaction was recently demonstrated to be important in HMF transformation [49], and must be taken into account when studying furanic aldehyde reactivity.

In order to verify the ability of the catalyst to convert different reaction intermediates, HMFCA, DFF and FFCA were separately used as reagents. After 30 min reaction time, a very low conversion of HMFCA was shown (Table 4 – entry 2), which confirms the inability of the calcined catalyst to activate this molecule; moreover, no products of degradation were detected, indicating that the molecule is stable even in strongly basic conditions, probably because of the absence of the aldehydic group.

The use of DFF as the reagent (Table 4 – entry 3) resulted in the total transformation of this compound into FFCA, thus proving that the latter may be directly derived from DFF oxidation. DFF was reported to be an intermediate in HMF oxidation, especially when the reaction is carried out in the absence of a base [21], but it was not detected in our standard tests. Nevertheless, when our catalyst was used in extremely mild conditions (reaction temperature 25°C, 10 min, $O_2$ pressure 10

bar, HMF:NaOH 1:1), a small amount of DFF was formed, together with HMFCA and FFCA, in agreement with previously reported results. In the presence of $O_2$, the formation of a small amount of HMF made it possible to conclude that the Cannizzaro disproportionation makes a small, but non-negligible, contribution to DFF conversion, while the oxidation reaction is kinetically much more favoured. Nevertheless, when the reaction was carried out under $N_2$, besides FFCA important amounts of HMF and degradation products were observed (Table 4 – entry 4), suggesting the significant contribution of DFF disproportionation to the formation of FFCA and HMF (Scheme 2).

Unexpectedly, the conversion of FFCA was very modest under both $O_2$ and $N_2$ (Table 4 – entries 5 and 6), indicating that the calcined $Pd_1Au_6$-$TiO_2$ was almost inactive in FFCA conversion. Therefore, FDCA cannot derive exclusively from either FFCA oxidation and/or disproportionation: some additional parallel pathway for its formation should be hypothesized.

Indeed, when some HMF was added to the reaction medium (with a HMF/FFCA molar ratio 1:1), HMFCA, FDCA and BHMF formed in significant amounts (Table 4 – entry 7), an event which indicates the presence of a different path for FFCA conversion and FDCA production. In fact, during HMF oxidation FFCA may react with residual HMF by means of a Cannizzaro-type reaction, and this cross-disproportionation may yield different products: either (a) two molecules of HMFCA, which is a stable compound (entry 2 in Table 4), or (b) one molecule of BHMF and one of FDCA; the former is soon oxidised to HMF and HMFCA (entry 8 in Table 4). In fact, the products formed in the co-feed experiment (entry 7 in Table 4) were HMFCA, FFCA, FDCA, and traces of BHMF. However, due to the fact that HMF is a very reactive molecule (even with the less active calcined catalyst), and therefore the concentration of residual HMF was very low, disproportionation of FFCA with DFF (leading either to FDCA + HMF, or to HMFCA + FFCA) might also have contributed to products formation. Whichever was the reaction involved, our experiments showed clearly (see Table 4) that a disproportionation-type reaction involving FFCA as the reactant was the only route leading to FDCA formation, while FFCA itself was very slowly oxidised to FDCA. The formation of the right amount of BHMF, as expected from this disproportionation, could not be ascertained, due to the rapid oxidation of the latter under the conditions used, as confirmed by the test reported in Table 4 (entry 8).

A summary of the main reaction pathways involved in HMF oxidation on calcined $Pd_1Au_6$-$TiO_2$ under basic conditions is shown in Scheme 3.

We also carried out reactivity experiments aimed at elucidating the role of the Cannizzaro disproportionation with the dried $Pd_1Au_6$-$TiO_2$ sample. Preliminary results using FFCA as the reagent under differential conditions suggested the predominance of the oxidative pathway for FDCA

formation, although a small contribution of the Cannizzaro reaction was detected; further studies are necessary to better clarify this point.

In conclusion, we demonstrated that the calcination treatment dramatically changed the reactivity of $Pd_1Au_6$-$TiO_2$, and altered the mechanism of FDCA formation from HMF. Indeed, this material was unable to oxidise molecules containing the –COOH functional group, such as HMFCA and FFCA.

*3.2.3 Test using non-supported nanoparticles*

PVP-protected Pd-Au nanoparticles with different structures (alloy and core-shell morphology) were tested as catalysts in order to confirm the presence of different mechanisms for FDCA formation in function of catalyst morphology. As previously reported, the synthesis of bimetallic Au(core)@Pd(shell) and Pd(core)@Au(shell) sols, with a Pd:Au molar ratio equal to 1:6, was carried out using the same method as for alloyed samples, but the second metal was added to the sol once the core-seed of the first metal had been formed. As detailed above, TEM, STEM and XEDS confirmed the expected distribution of metals within the nanoparticles; the synthetized sols were used as such in the reaction, without any support.

With the alloyed sol, the catalytic activity was very similar to that shown by the dried $Pd_1Au_6$-$TiO_2$ sample (Fig. 11), despite the different nanoparticles dimension (3.9 nm for sols and 6.0 for the supported sample). This indicates that the effect of nanoparticles size on the reaction mechanism is negligible if compared to the effect of morphology, at least in the range of particles size investigated. The oxidation of HMF progressed through the rapid formation of HMFCA, followed by the subsequent oxidation to FFCA and then to FDCA. HMF conversion was always complete and the alloy was more efficient in converting HMFCA (in contrast to what shown with the corresponding supported calcined catalyst), forming FDCA with 80% selectivity after 4 h reaction time. Similar results were obtained using the Pd@Au sol, preferentially exposing Au atoms on the nanoparticle surface (Fig.12), which appeared highly active in HMFCA formation and conversion. Conversely, the use of a Pd-shell catalyst (Au@Pd) showed a very different trend (Fig.13). The sample was active in the first steps of the reaction network, producing both HMFCA and FFCA. However, the catalyst was poorly active for the subsequent oxidation of these molecules, as previously also observed for both the monometallic Pd-$TiO_2$ and the calcined bimetallic catalyst; correspondingly, the selectivity to HMFCA, FFCA and FDCA remained almost unchanged between 60 and 240 min reaction time, which suggests that Au is the key catalytic component under basic conditions.

## Conclusions

The aerobic oxidation of 5-hydroxymethylfurfural in water over $TiO_2$-supported Au and Pd catalysts provides an environmentally benign route to 2,5-furandicarboxylic acid, an important compound serving as the starting point for the synthesis of bio-polymers.

Samples with different Pd:Au atomic ratio and morphology (alloy and core-shell) were prepared in order to investigate the effect of catalyst composition on catalytic activity and products selectivity. This study allowed us to conclude that the reaction network was strongly affected by catalyst composition. In fact, Pd-$TiO_2$ was poorly selective to FDCA, while the formation of the latter was strongly enhanced compared to Au-$TiO_2$ by alloying small amounts of Pd with Au. However, a thermal treatment of the supported Pd-Au alloy at 300°C led to the development of a catalyst whose behavior was similar to that shown by Pd-$TiO_2$, because of the segregation of Pd towards the outer part of the alloy nanoparticles, with Pd surface enrichment.

The reason for this behavior derived from the substantial inability of Pd and surface Pd-enriched alloys to oxidise the hydroxymethyl group of the intermediate compound, 5-hydroxymethyl furancarboxylic acid. With these catalysts, a different reaction pathway took place for 2,5-furandicarboxylic acid formation, involving a Cannizzaro-type reaction between the reactant, 5-hydroxymethylfurfural, and the intermediate compound, 5-formylfurancarboxylic acid. This mechanism was confirmed using core-shell nanoparticles, preferentially exposing either Au or Pd atoms.

## Acknowledgements

The University of Bologna is acknowledged for financial support through the FARB Project “Catalytic transformation of biomass-derived materials into high added-value chemicals”, 2014–2015. INSTM is acknowledged for co-financing the PhD project of A.L.

## References

[1] J. N. Chheda, G. W. Huber, J. A. Dumesic, Angew. Chem. Int. Ed. 46 (2007) 7164-7183.

[2] R. A. Sheldon, Green Chem. 16 (2014) 950-963.

[3]A. Corma, S. Iborra, A. Velty, Chem Rev 107 (2007) 2411 -2502.

[4] M. J. Climent, A. Corma, S. Iborra, Green Chem. 16 (2014) 516-547.

[5] J. N. Chheda, Y. Roman-Leshkov J. A. Dumesic, Green Chem. 9 (2007), 342-350.

[6] T. Werpy, G. Petersen, 2004 Top Value Added Chemicals From Biomass http://www1.eere.energy.gov/bioenergy/pdfs/35523.pdf

[7] F. Yang, Q. Liu, X. Bai, Y. Du, Bioresource Technol 102 (2011) 3424-3429.

[8] R. J. van Putten, J. C. van der Waal, D. De Jong, C. B. Rasrendra, H. J. Heeres, J. G. de Vries, Chem. Rev., 113 (2013) 1499-1597.
[9] C. Munoz de Diego, P. Shammel Wayne, A. Dam Matheus, J. M. Gruter Gerardus, WO Patent 2011/043660 (2011) assigned to Furanix Technologies BV.
[10] K. Yutake, T. Toshinari, S. Eritate, T. Komoro, US Patent 2011/092720 (2011) assigned to Canon KK.
[11] A. Shalkh, D. R. Parker, M. E. Janka, L. R. Partin, US Patent 2014/0142328 (2014) assigned to Eastman Chemical Company.
[12] Y. Y. Gorbanev, S. K. Klitgaard, J. M. Woodley, C. H. Christensen, A. Riisager, ChemSusChem, 2 (2009) 672-675.
[13] S. E. Davis, B. N. Zope, R. J. Davis, Green Chem. 14 (2012) 143-147.
[14] A. A. Rosatella, S. P. Simeonov, R. F. M Frade, C. A. M. Afonso, Green Chem. 13 (2011) 754-793.
[15] C. Moreau, M. N. Belgacem, A. Gandini, Top. Catal. 27 (2004) 11-30.
[16] J. Cai, H. Ma, J. Zhang, Q. Song, Z. Du, Y. Huang, J. Xu, Chem-Eur J. 19 (42) (2013) 14215-14223.
[17 ] N. K. Gupta, S. Nishimura, A. Takagaki, K. Ebitani, Green Chem. 13 (2011) 824-827.
[18] T. Pasini, M. Piccinini, M. Blosi, R. Bonelli, S. Albonetti, N. Dimitratos, J. A. Lopez-Sanchez, M. Sankar, Q. He, C. J. Kiely, G. J. Hutchings, F. Cavani, Green Chem. 13 (2011) 2091-2099.
[19] A. Villa, M. Schiavoni, S. Campisi, G. M. Veith, L. Prati, ChemSusChem 6 (2013) 609-612.
[20] S. Albonetti, T. Pasini, A. Lolli, M. Blosi, M. Piccinini, N. Dimitratos, J. A. Lopez-Sanchez, D. J. Morgan, A. F. Carley, G. J. Hutchings, F. Cavani, Catal. Today 195 (2012) 120-126.
[21] X. Wan, C. Zhou, J. Chen, W. Deng, Q. Zhang, Y. Yang, Y. Wang, ACS Catalysis 4 (2014) 2175-2185.
[22] A. Villa, D. Wang, D. Su, G. M. Veith, L. Prati, Phys. Chem. Chem. Phys. 12 (2010) 2183–2189.
[23] S. Nishimura, N. Ikeda, K. Ebitani, Catal. Today 232 (2014) 89–98
[24] N. Dimitratos, F. Porta, L. Prati, A. Villa, Catal. Letters 99 (3-4) (2005) 181-185.
[25] N. Dimitratos, F. Porta, L. Prati, Appl. Catal. A 291 (2005) 210-214.
[26] N. Dimitratos, A. Villa, D. Wang, F. Porta, D. Su, L. Prati, J. Catal. 244 (2006) 113–121.
[27] J. Pritchard, M. Piccinini, R. Tiruvalam, Q. He, N. Dimitratos, J. A. Lopez-Sanchez, D. J. Morgan, A. F. Carley, J K. Edwards, C. J. Kiely, G. J. Hutchings, Catal. Sci. Technol. 3 (2013) 308-317.

[28] J. A. Lopez-Sanchez, N. Dimitratos, N. Glanville, L. Kesavan, C. Hammond, J. K. Edwards, A. F. Carley, C. J. Kiely, G. J. Hutchings, Appl. Catal. A 391 (2011) 400–406.
[29] G. J. Hutchings, C. J. Kiely, Acc. Chem. Res. 46(8) (2013)1759–1772.
[30] A. A. Herzing, A. F. Carley, J. K. Edwards, G. J. Hutchings, C.J . Kiely, Chem. Mater. 20 (2008) 1492-1501.
[31] L. Delannoy, S. Giorgio, J. G. Mattei, C. R. Henry, N. El Kolly, C. Méthivier, C. Louis, ChemCatChem 5 (2013) 2707-2716.
[32] P. Raveendran, J. Fu, L. Wallen, Green Chem. 8 (2006) 34-38.
[33] J. Liu, G. Qin, P. Raveendran,Y. Ikushima, Chem. Eur. J. 12 *(*2005) 2131-2138.
[34] M. Blosi, S. Albonetti, M. Dondi, G. Baldi, A. Barzanti, PCT/EP2010/052534, 2010.
[35] M. Blosi, S. Albonetti, G. Baldi, F. Gatti, M. Dondi, Dyes Pigments 94 (2) (2012) 355-362.
[36] S. Albonetti, M. Blosi, F. Gatti, A. Migliori, L. Ortolani, V. Morandi, G. M. Baldi, Stud. Surf. Sci. Catal. 175 (2010) 621-624.
[37] M. Blosi, S. Albonetti, S. Ortelli, A.L. Costa, L. Ortolani, M. Dondi, New J. Chem. 38 (2014) 1401-1409.
[38] S. Albonetti, A. Lolli, V. Morandi, A. Migliori, C. Lucarelli, F. Cavani, Appl. Catal B 163 (2015) 520–530.
[39] O. Casanova, S. Iborra, A. Corma, ChemSusChem. 2 (2009) 1138-1144
[40] M.A. Lilga, R. T. Hallen, J. Hu, J. F. White, M.J. Gray, US 2010/0152470 (2010), assigned to Battelle Memorial Institute.
[41] S. E. Davis, L. R. Houk, E. C. Tamargo, A. K. Datye, R. J. Davis, Catal. Today 160 (2011) 55.
[42] S. E. Davis, A. D. Benavidez, R. W. Gosselink, J. H. Bitter, K. P. de Jong, A. K. Datye, R. J. Davis J. Mol. Catal. A: Chemical 388-389 (2014) 123-132.
[43] H. A. Rass, N. Essayem, M. Besson Green Chem. 15 (2013) 2240–2251.
[44] Z. Zhang, B. Liu, K. Lu, J. Sun, K. Deng Green Chem. 16 (2014) 2762-2770.
[45] A. Villa, D. Wang, D.S. Su, L. Prati, ChemCatChem. 1 (2009) 510-514.
[46] G. A. Somorjai, H. Frei, J.Y. Park, J. Am. Chem. Soc. 131 (2009) 16589-16605.
[47] D. I. Enache, J. K. Edwards, P. Landon, B. Solsona-Espriu, A. F. Carley, A. A. Herzing, M. Watanabe, C. J. Kiely, D. W. Knight, G. J. Hutchings Science 311 (2006) 362-365.
[48] P. Paalanen, B.M. Weckhuysen, M. Sankar Catal. Sci. Technol. 3 (2013) 2869-2880.
[49] S. Subbiah, S. P. Simeonov, J. M. S. S. Esperança, L. Paulo N. Rebelo, C. A. M. Afonso, Green Chem. 15 (2013) 2849-2853.

**Table 1 –** Structural parameters and chemical composition Au and Pd-Au supported on $TiO_2$.

| Catalyst | Total metal loading (wt.%) | Pd (wt.%) | Au (wt.%) | Molar ratio Pd:Au | Surface Area ($m^2/g$) |
|---|---|---|---|---|---|
| $Pd\text{-}TiO_2$ | 1.5 | 1.5 | 0 | - | 72 |
| $Pd_3Au_1\text{-}TiO_2$ | 1.5 | 0.93 | 0.57 | 3 | 73 |
| $Pd_1Au_1\text{-}TiO_2$ | 1.5 | 0.53 | 0.97 | 1 | 78 |
| $Pd_1Au_3\text{-}TiO_2$ | 1.5 | 0.23 | 1.27 | 0.33 | 79 |
| $Pd_1Au_6\text{-}TiO_2$ | 1.5 | 0.12 | 1.38 | 0.16 | 79 |
| $Pd_1Au_9\text{-}TiO_2$ | 1.5 | 0.08 | 1.42 | 0.11 | 83 |
| $Au\text{-}TiO_2$ | 1.5 | 0 | 1.5 | - | 82 |

**Table 2** – Average diameters of metallic nanosols estimated from XRD and TEM analysis.

| Sol | d-XRD (nm) | d-TEM (nm) |
|---|---|---|
| Pd | 4 | 2.5 |
| $Pd_3Au_1$ | 4 | 3 |
| $Pd_1Au_1$ | 5 | 3 |
| $Pd_1Au_3$ | 5 | 4 |
| $Pd_1Au_6$ | 5 | 4 |
| $Pd_1Au_9$ | 5 | 4 |
| Au | 5 | 5 |

**Table 3 –** Comparison of the selectivity to the reaction products obtained with Pd-$TiO_2$ and Au-$TiO_2$ catalysts in different reaction conditions. Reaction time 240 min, $O_2$ pressure 10 bar. HMF:Metal molar ratio 1:0.01.

| Entry | Catalyst | NaOH/HMF molar ratio | T (°C) | HMF Conv (%) | HMFCA Sel. (%) | FDCA Sel.(%) | FFCA Sel. (%) | By-products Sel. (%) |
|---|---|---|---|---|---|---|---|---|
| **1** | $TiO_2$ | 2 | 70 | 74 | 20 | 0 | 0 | 80 |
| **2** | | 4 | 70 | 100 | 10 | 0 | 0 | 90 |
| **3** | Pd-$TiO_2$ | 0 | 70 | 0 | 0 | 0 | 0 | 0 |
| **4** | | 0.5 | 70 | 54 | 100 | 0 | 0 | 0 |
| **5** | | 2 | 70 | 100 | 92 | 8 | 0 | 0 |
| **6** | | 4 | 70 | 100 | 92 | 8 | 0 | 0 |
| **7** | | 2 | 90 | 100 | 91 | 9 | 0 | 0 |
| **8** | Au-$TiO_2$ | 2 | 70 | 100 | 86 | 12 | 2 | 0 |
| **9** | | 4 | 70 | 100 | 81 | 19 | 0 | 0 |
| **10** | | 2 | 90 | 100 | 78 | 13 | 9 | 0 |

**Table 4 –** Reactivity experiments from reaction intermediates over calcined $Pd_1Au_6$-$TiO_2$ catalyst. Reaction conditions: temperature 70°C, reaction time 30 min, $O_2$ pressure 10 bar, HMF:Metal:NaOH molar ratio 1:0.01:2.

| Entry | Reagent | Conv. (%) | FDCA Yield (%) | HMFCA Yield (%) | FFCA Yield(%) | HMF Yield(%) | BHMF Yield(%) | DFF Yield(%) | By-products Yield(%) |
|---|---|---|---|---|---|---|---|---|---|
| 1 | HMF (under $N_2$) | 57 | 0 | 0 | 0 | - | 0 | 0 | 57 |
| 2 | HMFCA | 3 | 0 | - | 0 | 0 | 0 | 0 | 3 |
| 3 | DFF | 96 | 1 | 1 | 88 | 6 | 0 | - | 0 |
| 4 | DFF (under $N_2$) | 55 | 0 | 1 | 22 | 14 | 0 | - | 18 |
| 5 | FFCA | 11 | 1 | 0 | - | 0 | 0 | 0 | 10 |
| 6 | FFCA (under $N_2$, no catalyst) | 0 | - | - | - | - | - | - | - |
| 7 | FFCA + HMF | -11 FFCA; 47 HMF | 6 | 26 | 11 | - | 1 | 0 | 3 |
| 8 | BHMF | 70 | 2 | 20 | 9 | 34 | - | 2 | 3 |

**Scheme 1** – General reaction network for HMF oxidation.

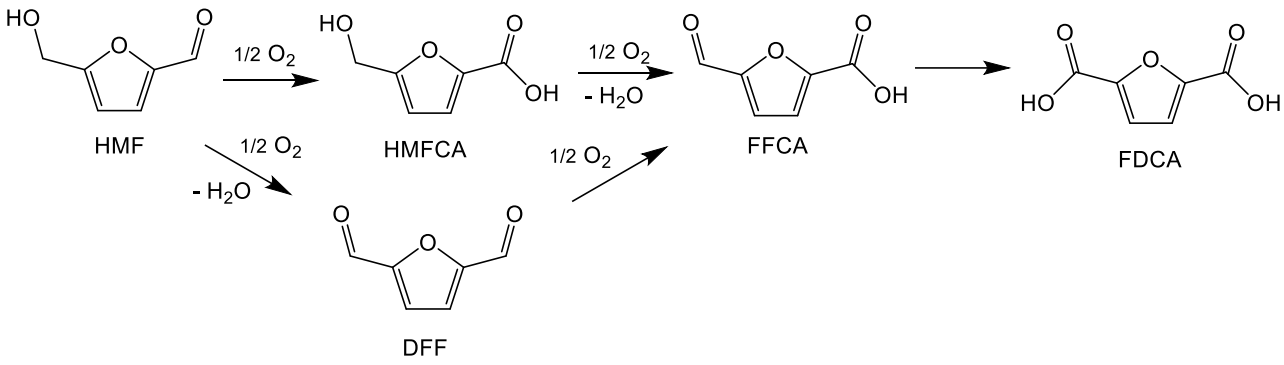


**Scheme 2 -** Cannizzaro reaction of DFF under inert atmosphere in the presence of a base.

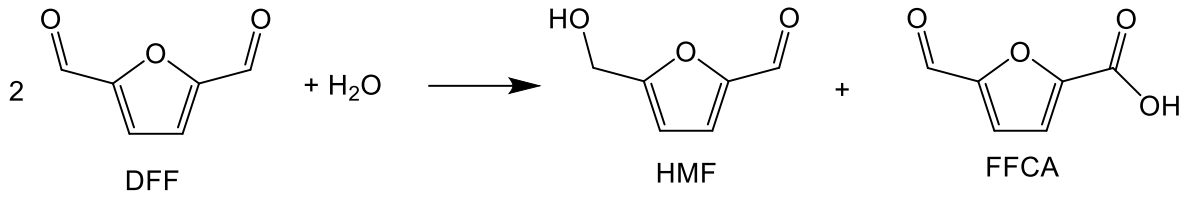


**Scheme 3 –** Main reaction pathways for the oxidation of HMF on calcined $Pd_1Au_6$-$TiO_2$ catalyst.

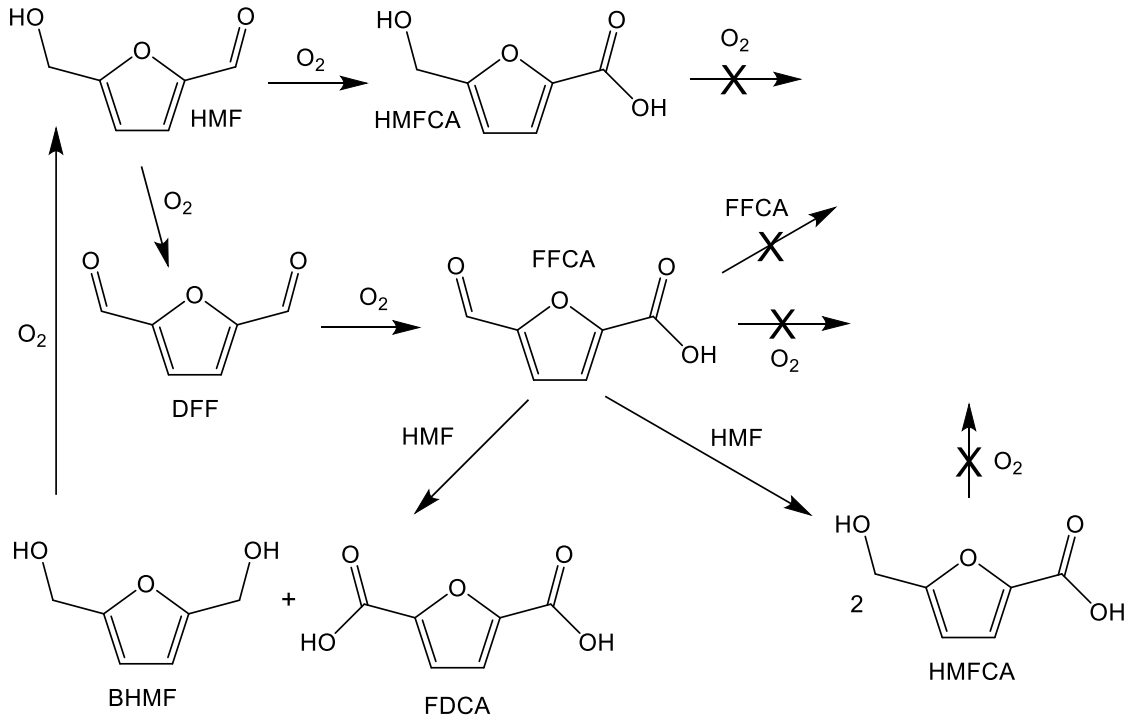

## Figures

**Figure 1 –** HR-TEM images and particle size distribution of the nanoparticle suspensions: a) Pd, b) $Pd_1Au_1$, c) $Pd_1Au_6$.

**Figure 2** – XRD patterns of the Pd-Au nanoparticles with the expected positions for the Pd(111) and Au(111) peaks indicated by broken lines. Legend: (a) Au; (b) $Pd_1Au_9$; (c) $Pd_1Au_6$; (d) $Pd_1Au_3$; (e) $Pd_1A_1$; (f) $Pd_3Au_1$; (g) Pd;

**Figure 3** – TEM images and particle size distribution of the $Pd_1@Au_6$ (Pd core) sample (a) and STEM image along with the corresponding Au-Lα, Au-Mα, Pd-Kα, Pd-Lα and (Au-L & Pd-K) elemental maps from the same area (b) (For interpretation of the reference to colour in this figure, the reader is referred to the Web version of the article).

**Figure 4** – TEM images and particle size distribution of the sample $Au_6@Pd_1$ (Au core) (a) and STEM image along with the corresponding Au-Lα, Au-Mα, Pd-Kα, Pd-Lα and (Au-L & Pd-K) elemental maps from the same area (b). (For interpretation of the reference to colour in this figure, the reader is referred to the Web version of the article).

**Figure 5** – TEM images and particle size distribution of the $Au_6Pd_1$ (alloy sample) (a) and STEM image along with the corresponding Au-Lα, Au-Mα, Pd-Kα, Pd-Lα, and (Au-L & Pd-K) elemental maps from the same area (b). (For interpretation of the reference to colour in this figure, the reader is referred to the Web version of the article).

**Figure 6** – HR-TEM images and particle size distribution of the dried catalysts: a) Pd-$TiO_2$ dried; b) $Pd_1Au_6$-$TiO_2$ dried; c) $Pd_1Au_6$-$TiO_2$ calcined.

**Figure 7** – Reaction profile for oxidation of HMF on Pd-$TiO_2$ (dried at 120°C). Reaction conditions: temperature 70°C, $O_2$ pressure 10 bar, HMF:Metal:NaOH molar ratio 1:0.01:2. Legend: ♦ HMF conversion, ■ HMFCA selectivity, ▲ FDCA selectivity.

**Figure 8** – Product selectivity on catalysts at different Pd:Au atomic ratios. Results are given at total conversion of HMF. Reaction conditions: temperature 70°C, $O_2$ pressure 10 bar, reaction time 240 min, HMF:Metal:NaOH molar ratio 1:0.01:2. Legend: ■ HMFCA, ▲ FDCA, X FFCA

**Figure 9** – HMF conversion and product selectivities as a function of time on $Pd_1Au_6$-$TiO_2$ sample dried at 120°C. Reaction conditions: temperature 70°C, $O_2$ pressure 10 bar, HMF:Metal:NaOH molar ratio 1:0.01:2. Legend: ♦ HMF conversion, ■ HMFCA selectivity, ▲ FDCA selectivity, X FFCA selectivity. The insert shows the final mixture at different reaction times.

**Figure 10 -** HMF conversion and product selectivities as a function of time on $Pd_1Au_6$-$TiO_2$ sample calcined at 300°C. Reaction conditions: temperature 70°C, $O_2$ pressure 10 bar, HMF:Metal:NaOH molar ratio 1:0.01:2. Legend: ♦ HMF conversion, ■ HMFCA selectivity, ▲ FDCA selectivity, X FFCA selectivity.

**Figure 11 –** HMF conversion and product selectivities as a function of time on unsupported $Pd_1Au_6$ alloy nanoparticle. Reaction conditions: temperature 70°C, $O_2$ pressure 10 bar, HMF:Metal:NaOH molar ratio 1:0.01:2. Legend: ♦ HMF conversion, ■ HMFCA selectivity, ▲ FDCA selectivity, X FFCA selectivity.

**Figure 12** – HMF conversion and product selectivities as a function of time on unsupported $Pd_1@Au_6$ core-shell nanoparticles. Reaction conditions: temperature 70°C, $O_2$ pressure 10 bar, HMF:Metal:NaOH molar ratio 1:0.01:2. Legend: ♦ HMF conversion, ■ HMFCA selectivity, ▲ FDCA selectivity, X FFCA selectivity.

**Figure 13** – HMF conversion and product selectivities as a function of time on unsupported $Au_6@Pd_1$ core-shell nanoparticles. Reaction conditions: temperature 70°C, $O_2$ pressure 10 bar, HMF:Metal:NaOH molar ratio 1:0.01:2. Legend: ♦ HMF conversion, ■ HMFCA selectivity, ▲ FDCA selectivity, X FFCA selectivity.

**Figure 1**

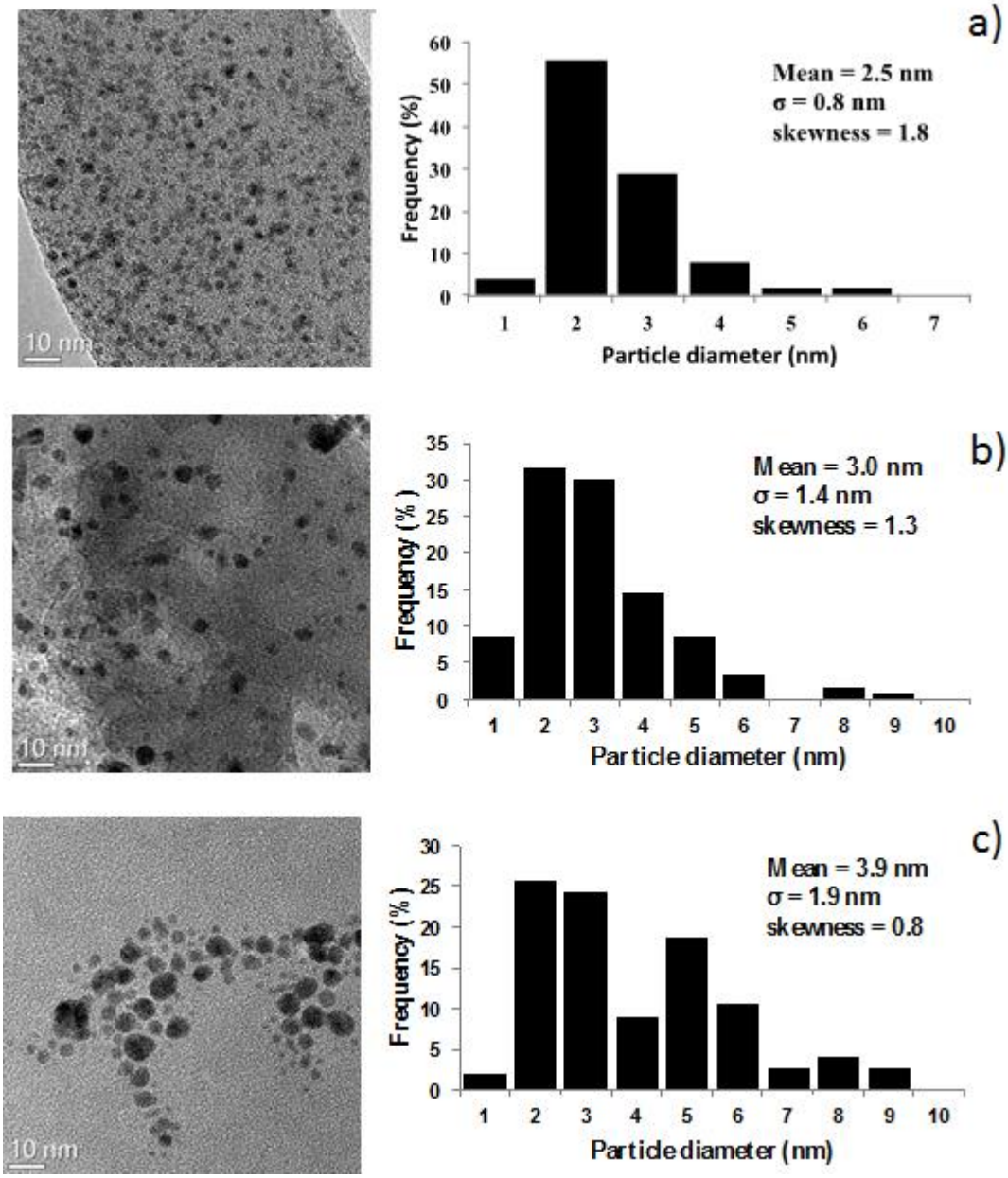
a)
10 nm
Frequency (%)
Mean = 2.5 nm
σ = 0.8 nm
skewness = 1.8
Particle diameter (nm)
b)
10 nm
Frequency (%)
Mean = 3.0 nm
σ = 1.4 nm
skewness = 1.3
Particle diameter (nm)
c)
10 nm
Frequency (%)
Mean = 3.9 nm
σ = 1.9 nm
skewness = 0.8
Particle diameter (nm)

**Figure 2**

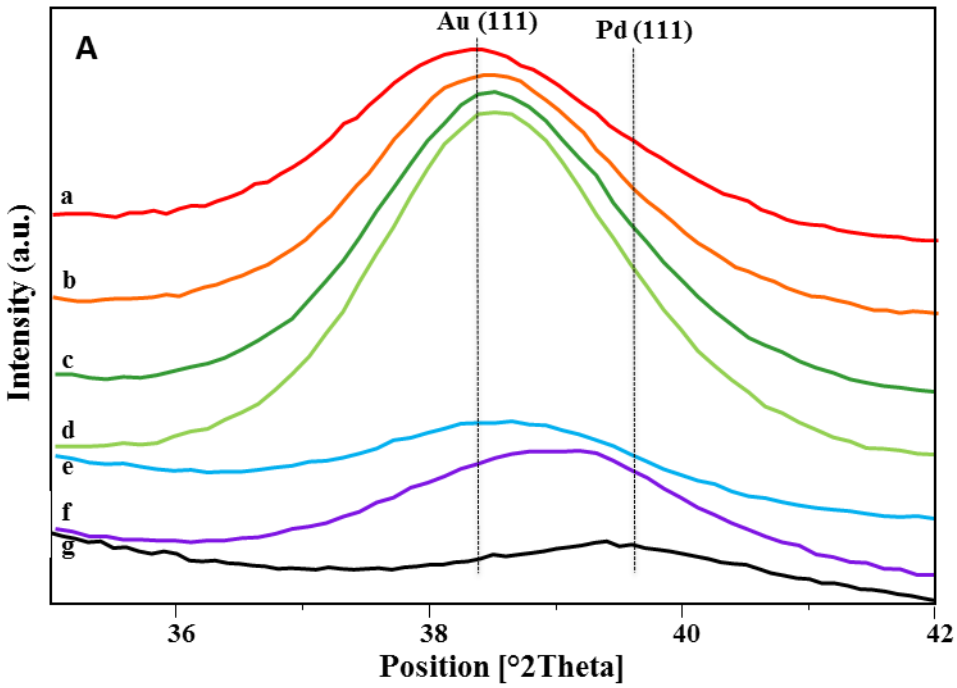
A
Au (111)
Pd (111)
a
b
c
d
e
f
g
Intensity (a.u.)
36
38
40
42
Position [°2Theta]

**Figure 3**

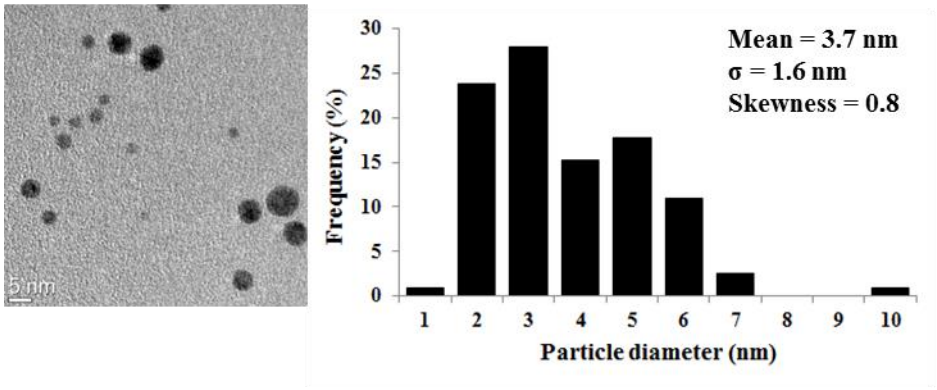
5 nm
Frequency (%)
30
25
20
15
10
5
0
1
2
3
4
5
6
7
8
9
10
Particle diameter (nm)
Mean = 3.7 nm
σ = 1.6 nm
Skewness = 0.8

a)

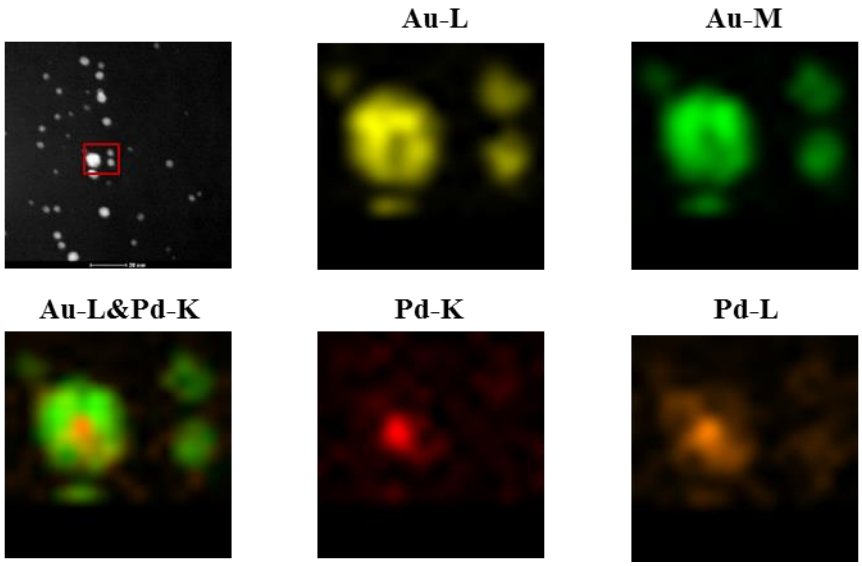
Au-L
Au-M
Au-L&Pd-K
Pd-K
Pd-L

b)

**Figure 4**

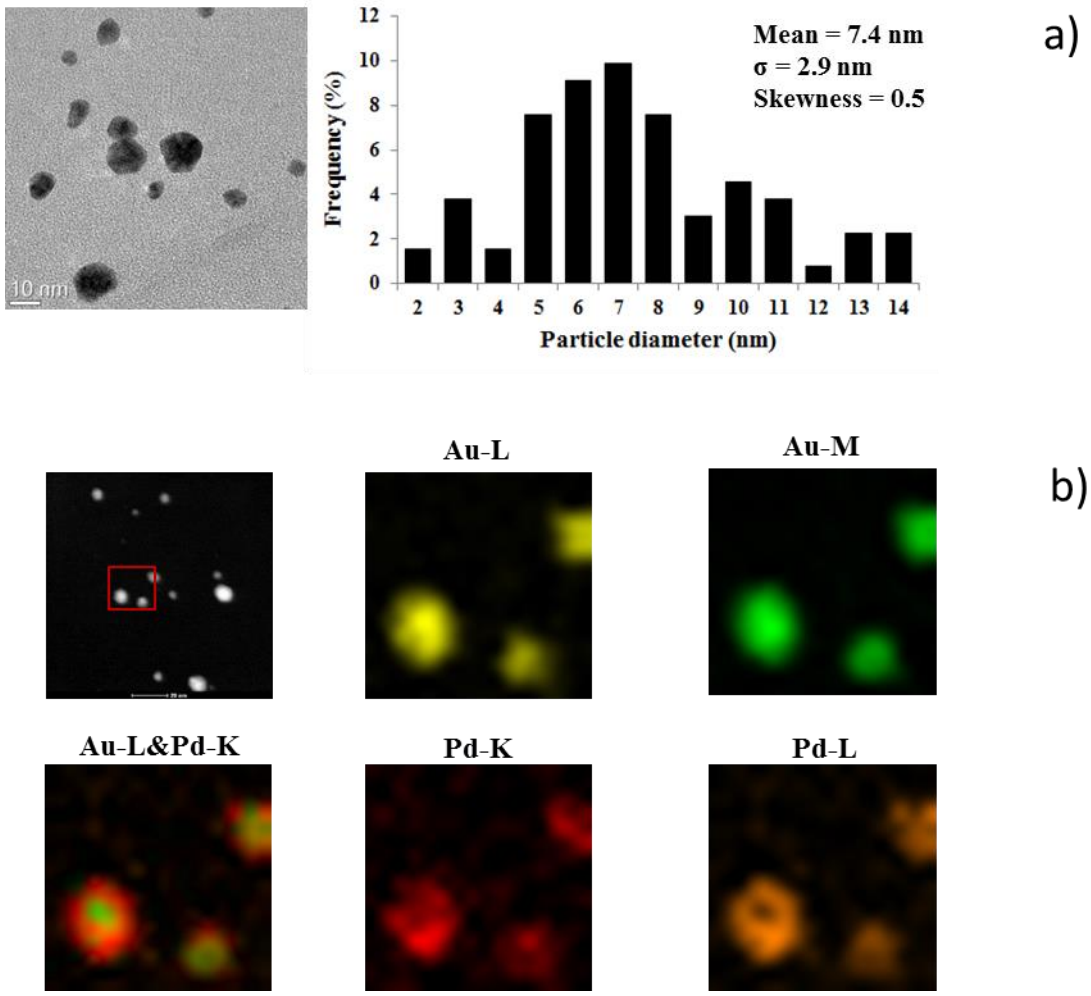
a)
10 nm
Mean = 7.4 nm
σ = 2.9 nm
Skewness = 0.5
Frequency (%)
Particle diameter (nm)
b)
Au-L
Au-M
Au-L&Pd-K
Pd-K
Pd-L

**Figure 5**

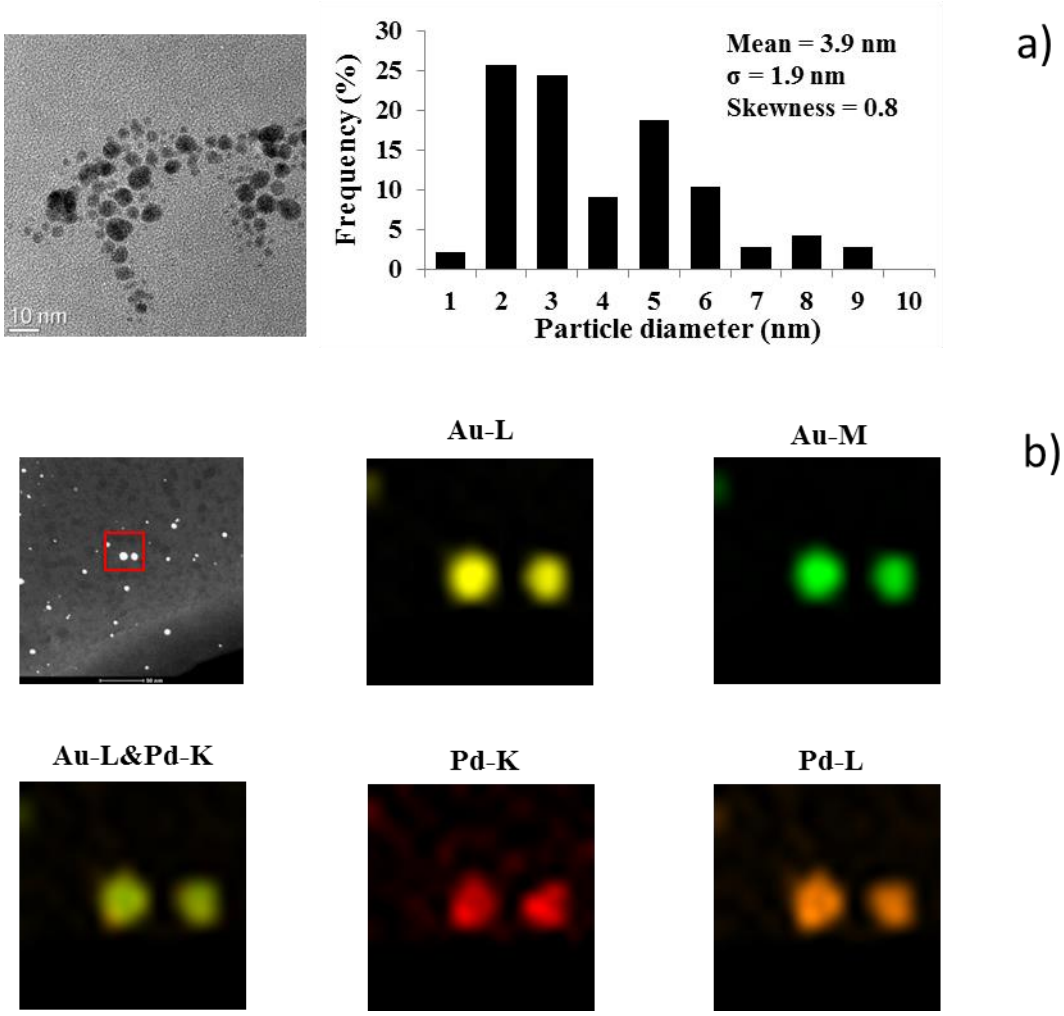
10 nm
Frequency (%)
30
25
20
15
10
5
0
1 2 3 4 5 6 7 8 9 10
Particle diameter (nm)
Mean = 3.9 nm
σ = 1.9 nm
Skewness = 0.8
a)
b)
Au-L
Au-M
Au-L&Pd-K
Pd-K
Pd-L

**Figure 6**

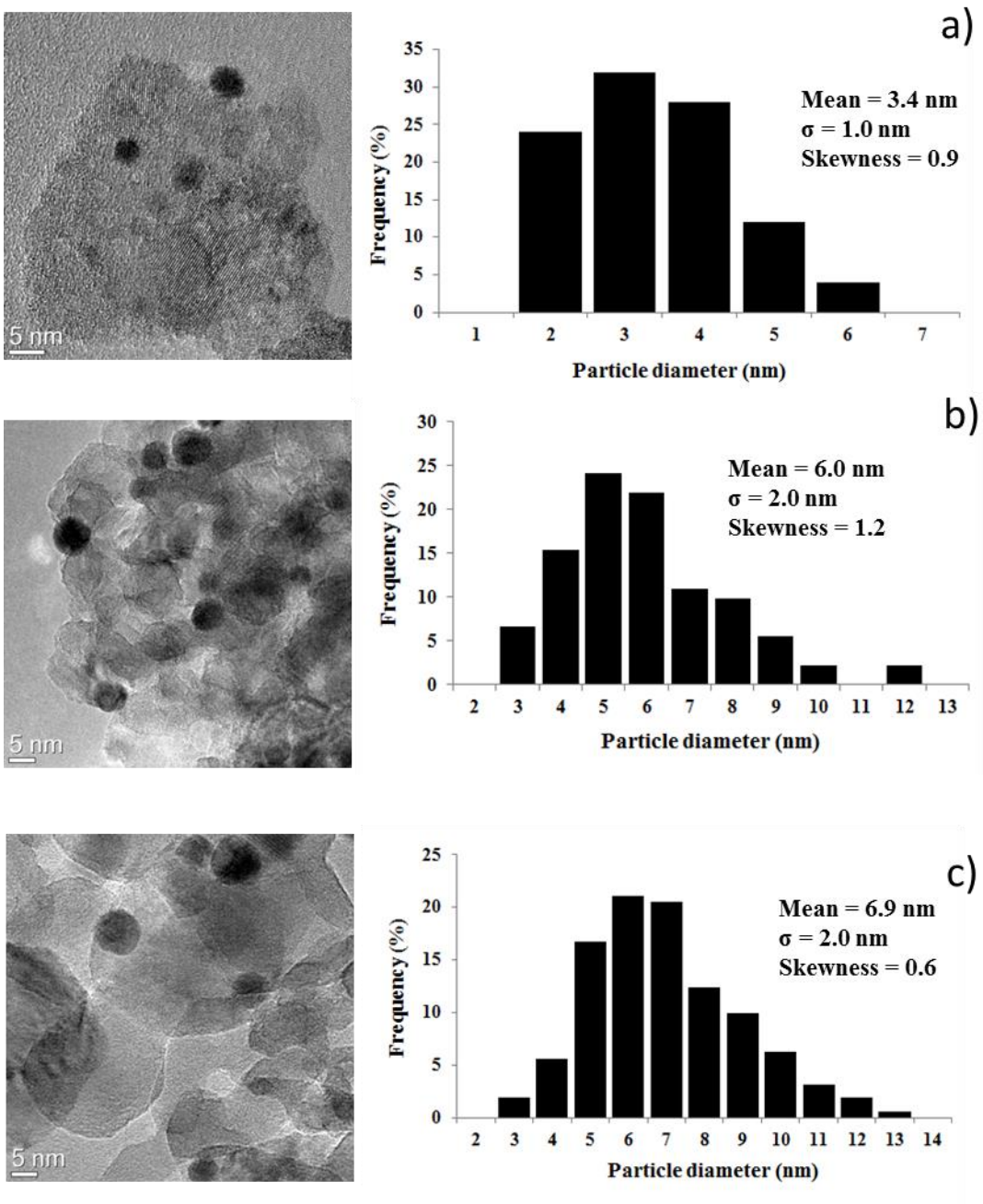
a)
5 nm
Frequency (%)
Particle diameter (nm)
Mean = 3.4 nm
σ = 1.0 nm
Skewness = 0.9
b)
5 nm
Frequency (%)
Particle diameter (nm)
Mean = 6.0 nm
σ = 2.0 nm
Skewness = 1.2
c)
5 nm
Frequency (%)
Particle diameter (nm)
Mean = 6.9 nm
σ = 2.0 nm
Skewness = 0.6

**Figure 7**

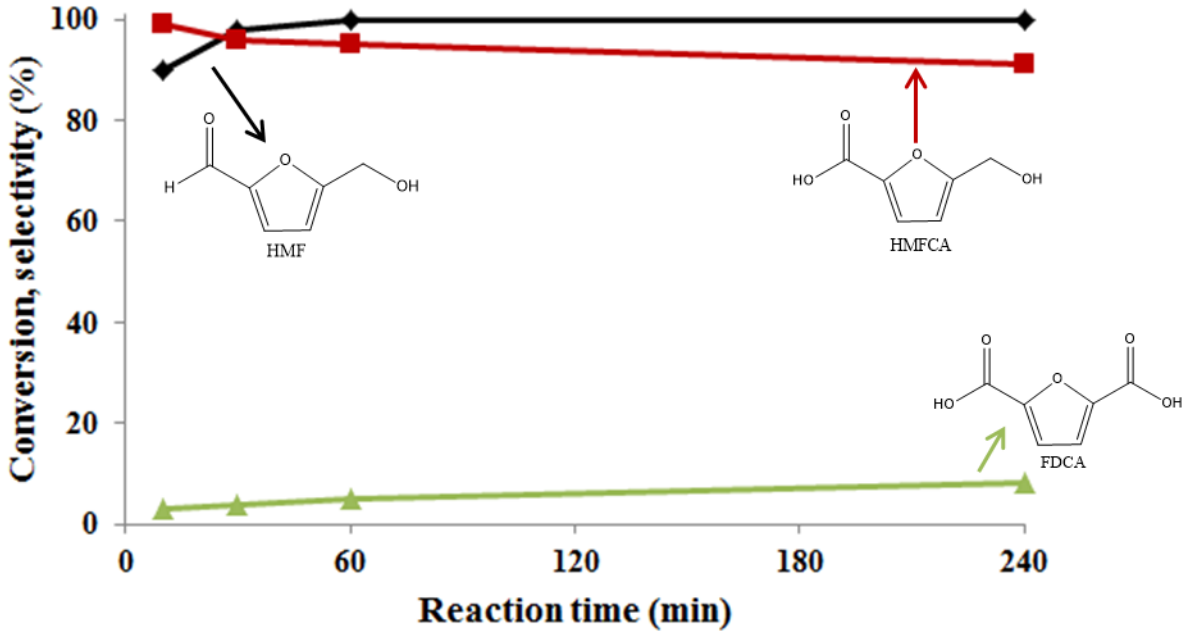
Conversion, selectivity (%)
100
80
60
40
20
0
0
60
120
180
240
Reaction time (min)
HMF
HMFCA
FDCA

**Figure 8**

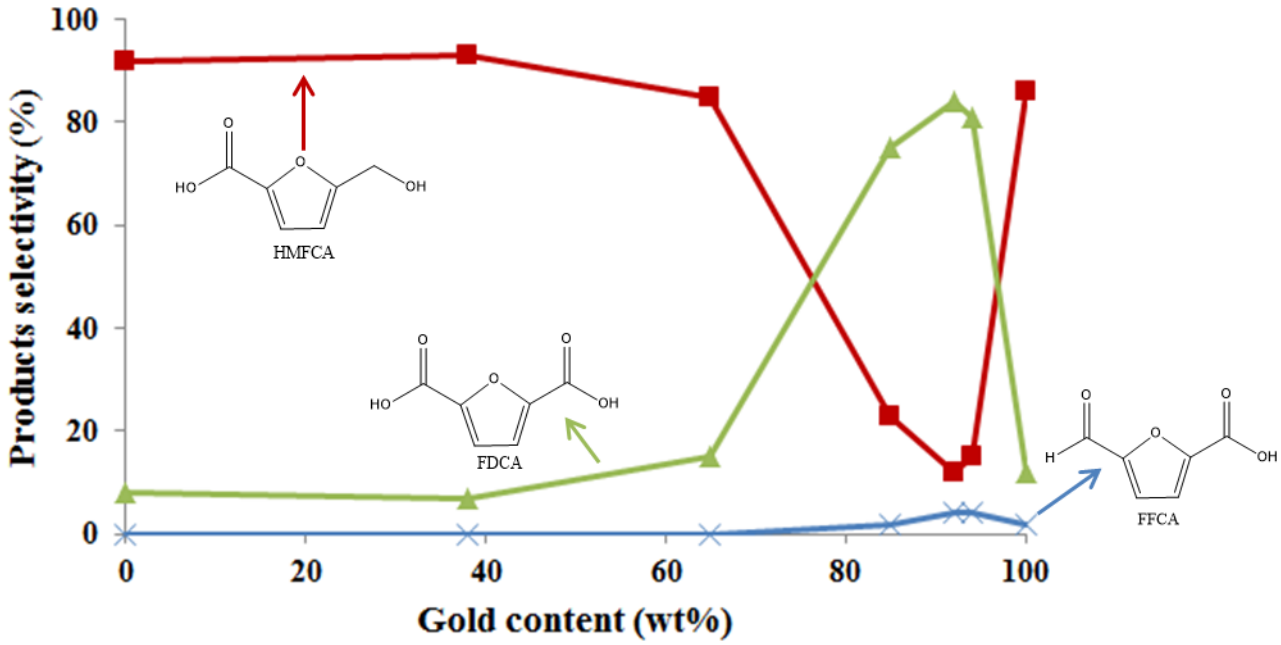
Products selectivity (%)
100
80
60
40
20
0
0
20
40
60
80
100
Gold content (wt%)
HMFCA
FDCA
FFCA

**Figure 9**

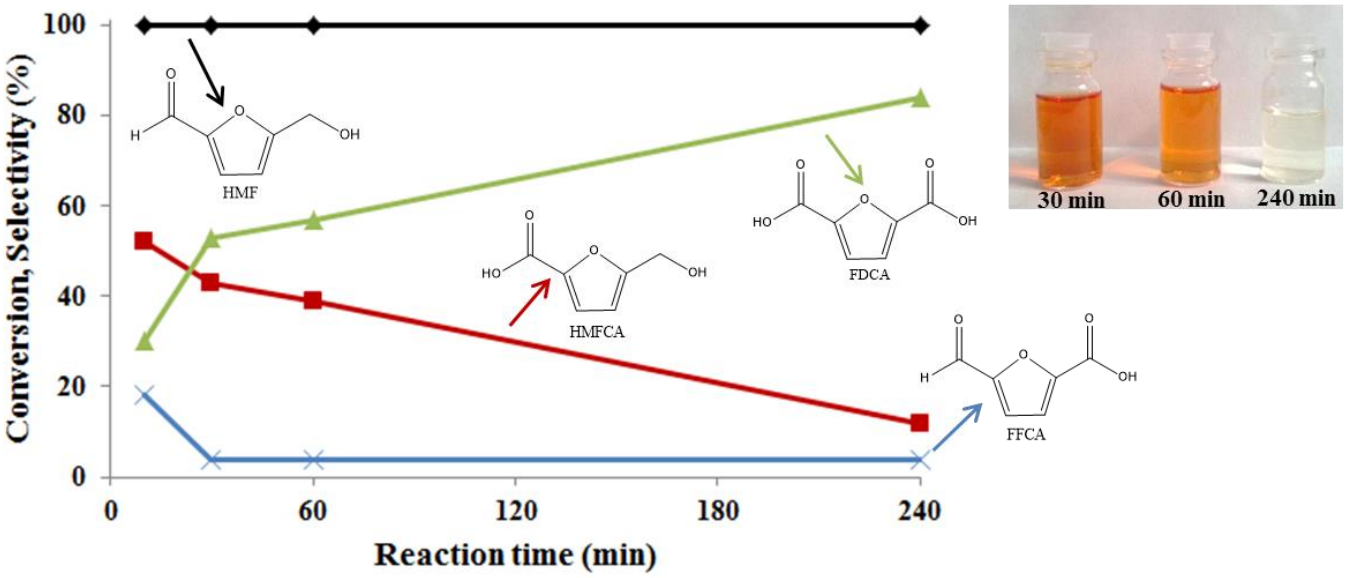
Conversion, Selectivity (%)
100
80
60
40
20
0
0
60
120
180
240
Reaction time (min)
HMF
HMFCA
FDCA
FFCA
30 min
60 min
240 min

**Figure 10**

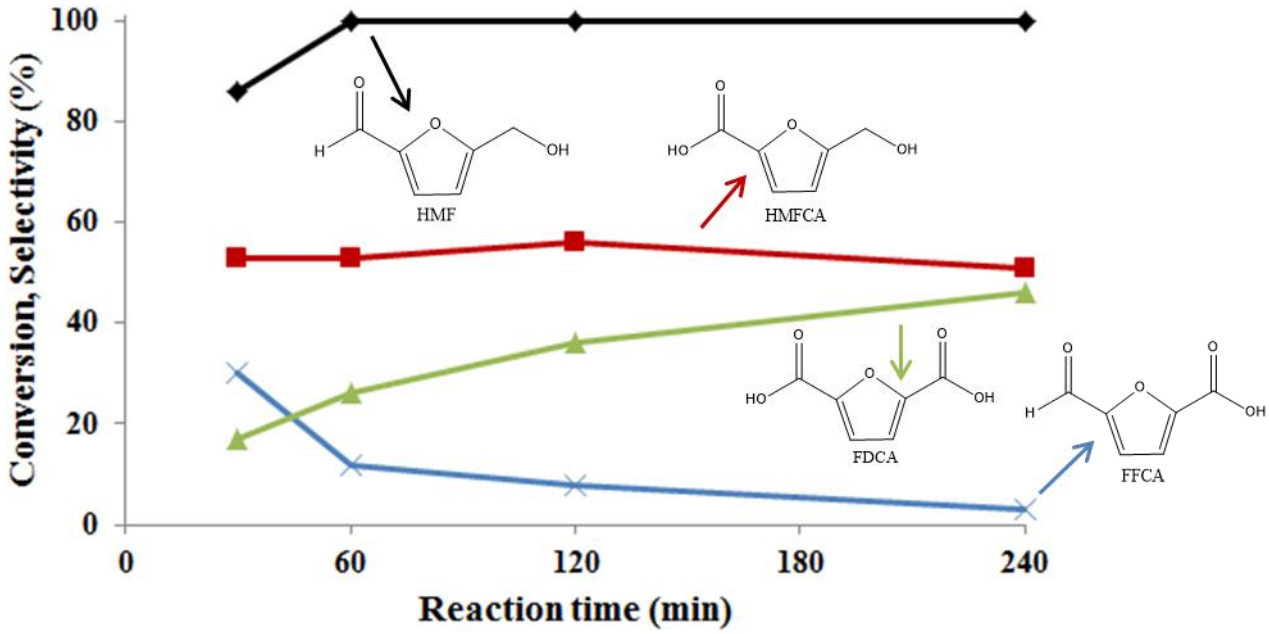
Conversion, Selectivity (%)
100
80
60
40
20
0
0
60
120
180
240
Reaction time (min)
HMF
HMFCA
FDCA
FFCA

**Figure 11**

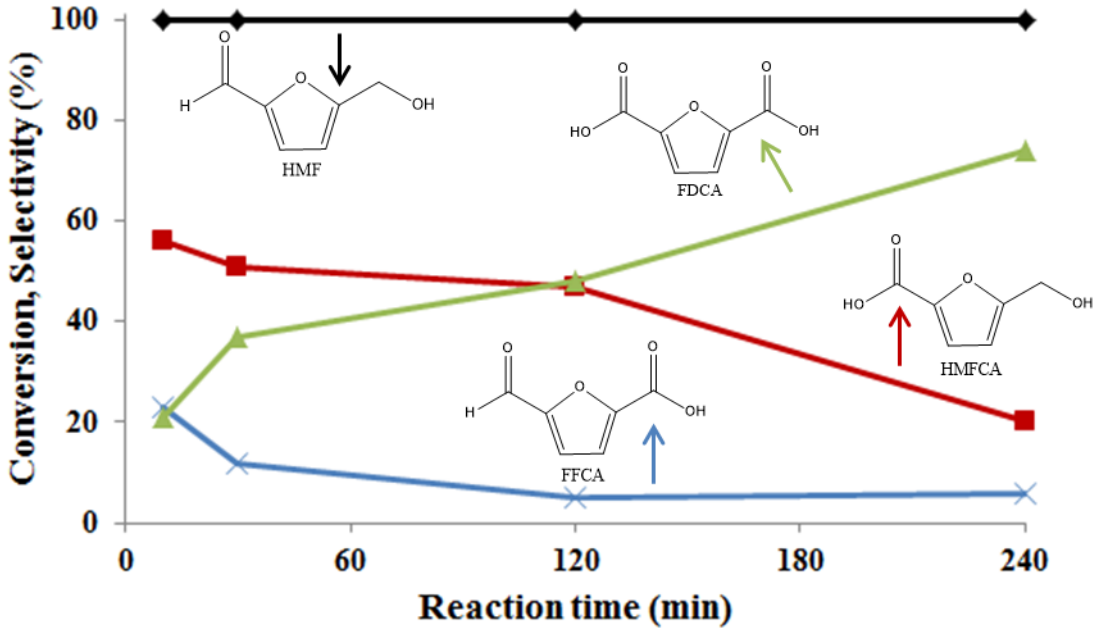
Conversion, Selectivity (%)
100
80
60
40
20
0
0
60
120
180
240
Reaction time (min)
HMF
FDCA
HMFCA
FFCA

**Figure 12**

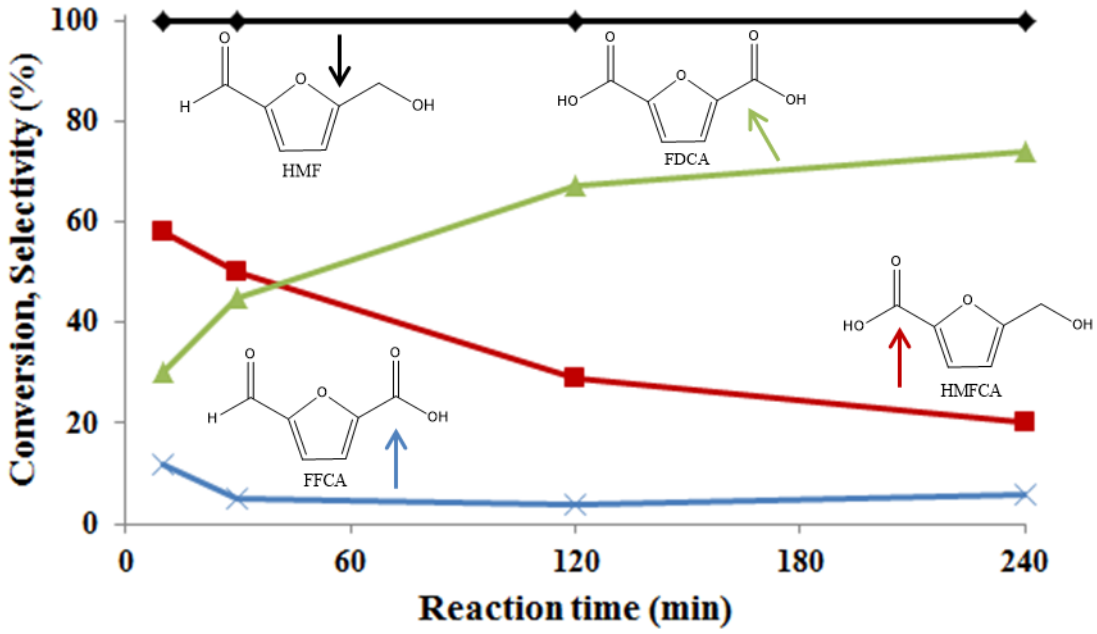
Conversion, Selectivity (%)
100
80
60
40
20
0
0
60
120
180
240
Reaction time (min)
HMF
FDCA
HMFCA
FFCA

**Figure 13**

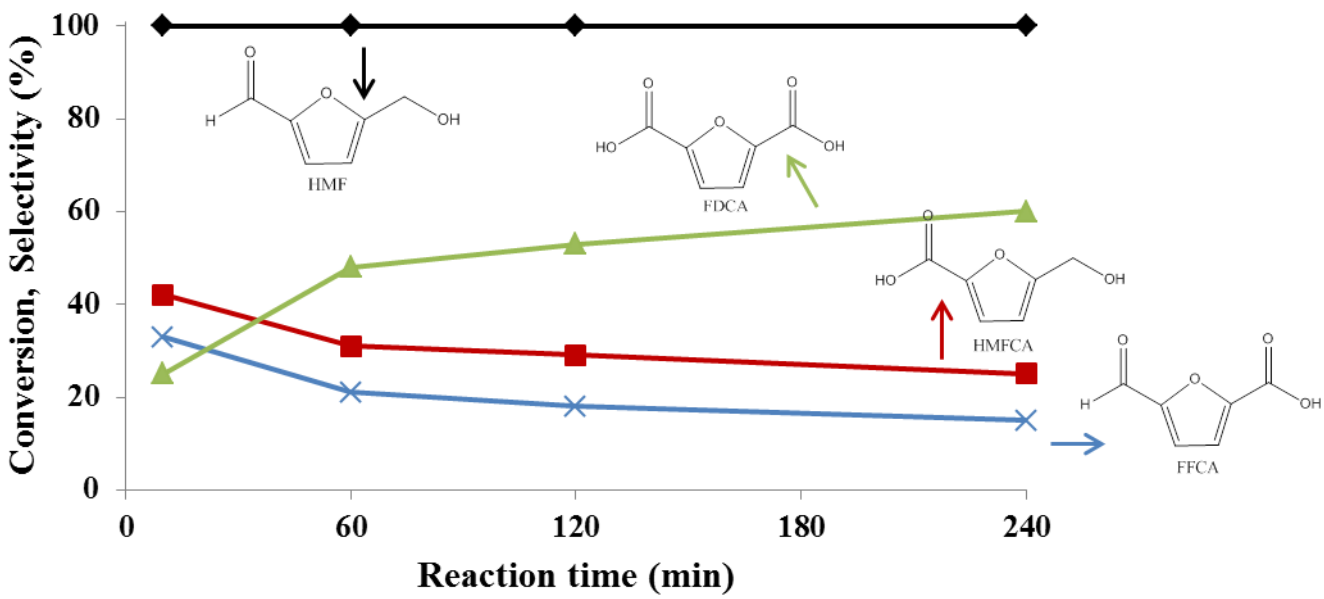
Conversion, Selectivity (%)
100
80
60
40
20
0
0
60
120
180
240
Reaction time (min)
HMF
FDCA
HMFCA
FFCA